Environmental Science and Pollution Research (2024) 31:49342–49357
https://doi.org/10.1007/s11356-024-34235-4

RESEARCH ARTICLE

ZnO/PUF composites with a large capacity for phosphate adsorption: adsorption behavior and mechanism studies

Yang Cao[1] · Peicong Zhang[1,2] · Suying Chen[1] · Yi Huang[2,3] · Junfeng Li[1] · Haiying Du[3] · Wentao Zhang[1] · Xianfei Chen[1] · Daming Yu[4]

Received: 16 December 2023 / Accepted: 30 June 2024 / Published online: 27 July 2024

Abstract

Phosphate is present in all kinds of industrial wastewater; how to remove it to meet the strict total phosphorus discharge standards is a challenge. This study used a one-step foaming technique to fill polyurethane foam (PUF) with ZnO, taking advantage of PUF's excellent features like its porous network, lightweight, hydrophilicity, and abundance of binding sites to create ZnO/PUF composites with high adsorption capacity and exceptional separation properties. The adsorption isotherms, kinetics, starting pH, and matrix impacts of ZnO/PUF composites on phosphate were examined in batch studies. The results showed that the composites had good adsorption performance for phosphate with a saturated adsorption capacity of 460.25 mg/g. The quasi-secondary kinetic and Langmuir models could better describe the adsorption process, which belonged to the chemical adsorption of monomolecular layers. The composites' ability to treat phosphates in complicated waters was shown by their ability to retain a high adsorption capacity in the pH range of 3–6. In column experiments, the composite also maintains a good affinity for phosphate during dynamic adsorption. Multiple characterizations indicate that the adsorption mechanism is a combined effect of ligand exchange and electrostatic interactions. Therefore, this study provides valuable insights for practical phosphorus-containing wastewater treatment.

Keyword ZnO/PUF · Phosphate · Adsorption

Introduction

Phosphorus is a non-renewable resource extensively utilized in agriculture, medicine, ceramics, and other industries. It is also necessary for human growth and development and for other creatures (Cordell et al. 2009; Cramer

Responsible Editor: Angeles Blanco

✉ Peicong Zhang
zhangpeicong@cdut.cn

Yang Cao
1436896597@qq.com

Suying Chen
2562969937@qq.com

Yi Huang
huangyi@cdut.cn

Junfeng Li
lijunfeng@cdut.edu.cn

Haiying Du
diane201109@126.com

Wentao Zhang
zhangwentao2012@cdut.cn

Xianfei Chen
chenxianfei2014@cdut.edu.cn

Daming Yu
420140730@qq.com

[1] College of Materials and Chemistry and Chemical Engineering, Chengdu University of Technology, Chengdu 610059, Sichuan, P.R. China

[2] State Key Laboratory of Geo-Hazard Prevention and Earth Environment Protection, Chengdu 610059, Sichuan, P.R. China

[3] College of Ecology and Environment, Chengdu University of Technology, Chengdu 610059, Sichuan, P.R. China

[4] Panzhihua Pangang Group Ming Company, Panzhihua 617000, Sichuan, P.R. China

2010). Unfortunately, phosphorus is currently wasted away as a significant amount is released into the environment annually through a variety of means, including the release of phosphorus-containing wastewater during phosphorus mining, the loss of phosphorus fertilizers in the soil during agricultural production, and phosphorus-containing domestic sewage. Orthophosphate is the primary fugitive form of phosphorus found in natural aquatic habitats (Zhang et al. 2020c). As phosphates collect sufficiently, the environment's phosphorus content increases significantly. Municipal wastewater discharge in China must not exceed 0.5 mg P/L. Permit limits in the USA must adhere to rigorous guidelines and fall between 0.1 and 0.5 mg P/L (Kumar et al. 2019). Overphosphorus in water may cause eutrophication, deplete the dissolved oxygen in the water, upset the ecosystem's balance, and endanger human health (Smith and Schindler 2009). As a result, there should be no delay in phosphorus removal from wastewater (Hwang 2020).

Presently, membrane filtration, adsorption, ion exchange, chemical precipitation, and other treatment techniques have all been employed to treat wastewater containing phosphorus (Ramasahayam et al. 2014; Hong et al. 2022; Zhang et al. 2020a). Among these methods, adsorption is widely regarded as a cost-effective technique for separation owing to its straightforward operational procedures, notable efficacy, economical nature, and convenient recovery process (Lalley et al. 2016; Feng et al. 2022). In recent years, many common adsorbent materials have been employed to extract phosphate from wastewater. For instance, Jung et al. (2016) discovered that the biochar produced by pyrolyzing undressing at 400 °C has an adsorption ability of 32.58 mg/g for phosphate at 30 °C, and Yan et al (2010) suggested using column-supported bentonite that was hydroxy-aluminum, hydroxy-iron, or combination hydroxy-iron-aluminum for the removal of phosphates; the highest adsorption capacities of these bentonite types were 12.7, 11.2, and 10.5 mg/g, respectively. Both biochar and conventional clay materials lack sufficient adsorption capability. Hence, exploring novel materials that might effectively boost the capacity to remove elevated phosphate levels in wastewater is essential.

Lewis acid–base action gives the zinc oxide an intense preference for phosphate. For instance, Luo et al.'s (2015) ZnO powder had a saturated adsorption ability of 163.40 mg/g for phosphate at a pH of 6.2 ± 0.1 in the solution. Phosphate was successfully removed from dendritic eclogite-zinc oxide nanocomposites by Wei et al. (2021) by successfully coating ZnO nanoparticles on tubular eclogite through noncovalent hybridization. Li et al. (2018) used hydrothermal atomic layer deposition to create magnetic 3D Fe_3O_4@ZnO nanomaterials with uniform active sites to remove phosphate from water in the presence of a modest magnetic field. Isothermal line fitting demonstrated that the composite phosphate had a saturation adsorption capability of 100.3 mg/g. By using saccharothermal calcination, Madhusudan et al. (2024) produced effective and environmentally benign $ZnO/ZnFe_2O_4$ yolk-shell microspheres that had an optimal adsorption capacity of 103.2 mg P/g for phosphate. However, the drawbacks of using composites and powdered zinc oxide as adsorbents include their instability, propensity for agglomeration, and difficulty in separating from the water column upon adsorption (Cheng et al. 2018; Shen et al. 2022). Consequently, it is critical to look for a straightforward technique to enhance zinc oxide's stability, dispersion, and separation qualities.

Generally, combining ZnO nanoparticles with organic polymer carriers is an effective way to improve the above deficiencies. For example, loading ZnO onto functional matrices such as chitosan (Chandra Das et al. 2023), graphene oxide aerogel (Shen et al. 2022), and 3D carbon foam (Zhang et al. 2020b) can be used for adsorption separation and photocatalytic degradation. However, there is no significant research on mixing ZnO and polyurethane foam (PUF). PUF is a porous material with remarkable thermochemical stability, hydrophilicity, cost-effectiveness, numerous binding sites, large specific surface area, three-dimensional structure, and porous network (Ren et al. 2022). Because of these characteristics, PUF is the best substrate for holding ZnO. In this work, ZnO powder was incorporated into PUF using a one-step foaming technique to create ZnO/PUF composite materials (Fig. 1). The PUF has a porous matrix that exhibits notable permeability and favorable flow characteristics, hence facilitating the efficient mitigation of mass transfer hindrances during the process of adsorption. The even distribution of ZnO inside the polyurethane foam matrix results in an increased number of binding sites, significantly enhancing the adsorption capabilities. These properties provide a new means of treating phosphorus-containing wastewater in real life.

Experiments and methods

Materials

The chemicals employed in this investigation are all of reagent-grade purity and were used without being purified. Zinc nitrate hexahydrate was obtained from Sinopharm Chemical Reagent Co. Dipotassium hydrogen phosphate, ammonium molybdate tetrahydrate, sulfuric acid, hydrochloric acid, glycerol, and polyethylene glycol(PEG) (Mn = 4000) were procured from Chengdu Kolon Chemical Co. At the same time, the stannous octoate and sodium

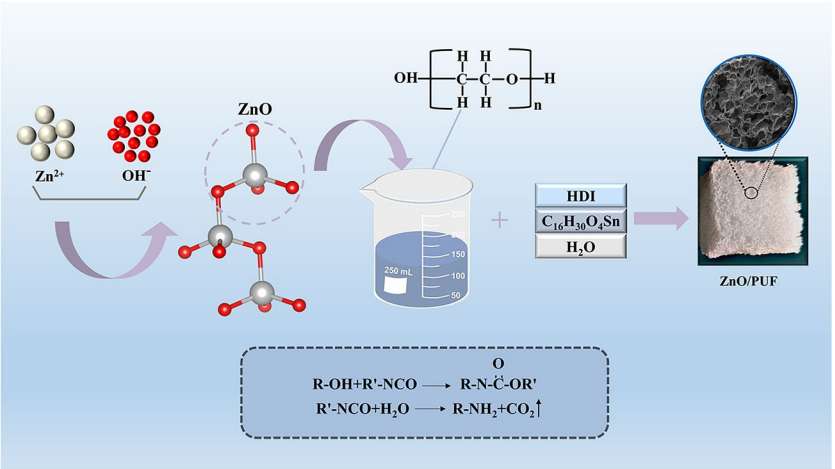

Fig. 1 Schematic diagram of the preparation of ZnO/PUF

hydroxide(HDI) were sourced from Beijing Inokai Technology Co.

Synthesis of ZnO

First, solution A with a concentration of 0.5 mol/L of Zn^{2+} was obtained by dissolving the necessary $Zn(NO_3)_2$ ($9H_2O$) in deionized water. Solution B was prepared by dissolving a certain quantity of NaOH in 120 mL of deionized water, per the molar ratio of Zn^{2+} to OH^- of 2:1. Subsequently, solution B was introduced into solution A uniformly. The sample was subjected to dynamic aging for 2 h on a magnetic stirring table with a temperature of 40 ℃. The samples were freeze-dried for 24 h to produce ZnO powder after being cleaned with deionized water and ethanol three times.

Preparation of ZnO/PUF

Twenty grams of PEG was put into a beaker and heated at 90 °C until melted. Then, 0–10 wt% of ZnO was added to the melt, and the mixture was obtained by stirring it evenly. Next, 0.5 mL of deionized water, 0.8 g of stannous octanoate, and HDI were added to the mixture all at once (n(PEG): n(HDI) = 1:3). After stirring and mixing the variety evenly, the reactants were put into a mold and allowed to foam for 30 s to produce the initial foam. The foam was matured in a warm oven at 100 °C over an hour, then cooled to room temperature to make the ZnO/PUF-s composites. The specific feed is shown in Table 1:

Table 1 The precise feed ratios

Products	PEG dosage/g	ZnO dosage/wt%
PUF	20	0
ZnO/PUF-2.5	20	2.5
ZnO/PUF-5	20	5.0
ZnO/PUF-7.5	20	7.5
ZnO/PUF-10	20	10.0

Characterization

The morphology of the materials was examined using a scanning electron microscope (SEM, S4800, Hitachi, Japan). Additionally, EDS spectroscopy was performed simultaneously with the morphological observations. The crystal structure of the samples was determined using an X-ray diffractometer (XRD, DX-2600, Danfang Dongyuan Instrument Co., Ltd., China). Fourier examined the infrared spectroscopy's functional groups transform (FTIR, TENSOR-27, Bruker GMBH, Germany). X-ray photoelectron spectroscopy (XPS, Escalab Xi+, Thermo Fisher Scientific, USA) analyzed the elemental state of the samples. The sample's thermal stability was evaluated using a thermogravimetric analyzer (TG/DTG, STA449F5, NETZSCH Instruments GmbH, Germany) in an inert environment. The samples' Zeta potential was determined using a Zeta potential analyzer (Zeta, Nano ZS90, Malvern Instruments Ltd, UK).

Batch experiments

The batch tests were conducted to investigate the adsorption characteristics of ZnO/PUF composites for phosphate. A phosphate-contaminated solution with a volume of 50 mL was combined with 0.5 g PUF and 0.5 g ZnO/PUF-s, correspondingly. The adsorption process took 1440 min, and the supernatant was collected. Phosphomolybdenum blue spectrophotometry was used to measure the phosphate concentration at 706 nm (Yuchi et al. 2003; He and Honeycutt

2005). Figure 2 illustrates the relationship between the measured spectrophotometric values and PO_4^{3-}. The following formulas (1 and 2) were used to determine the adsorption capacity per unit (estimated by ZnO) and the phosphorate removal rate.

$$Q_e = \frac{(C_0 - C_e)V}{m} \tag{1}$$

$$R = \frac{C_0 - C_e}{C_0} \times 100\% \tag{2}$$

where C_0 and C_e represent the initial and equilibrium concentrations of phosphate solution (mg/L), respectively, V is the phosphate solution volume (mL), and m is the adsorbent mass (g). R is the removal rate of phosphate.

Adsorption isotherm experiments

A solution containing varying concentrations of phosphate (10 mg/L, 20 mg/L, 30 mg/L, 40 mg/L, 60 mg/L, 80 mg/L, 100 mg/L, 120 mg/L, 150 mg/L, 200 mg/L, 300 mg/L, 500 mg/L, 800 mg /L, and 1000 mg/L) was mixed with 0.5 g of ZnO/PUF-5. The mixture was then adsorbed at 25 °C for 1440 min, and the initial pH of the contaminated solution was 6.3. The phosphate batch adsorption tests on ZnO/PUF-5 composites at varied starting concentrations were used to derive the adsorption isotherm data. The experimental data was fitted using the Langmuir, Freundlich, Temkin, and Redlich-Peterson isotherm models (3–6) (Huang et al.2015):

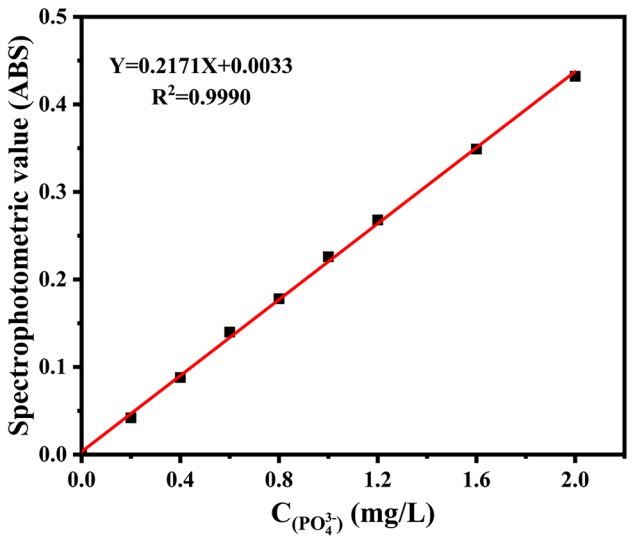

Fig. 2 Standard curve of phosphate concentration

$$\text{Langmuir model}: Q_e = \frac{Q_m K_L C_e C_0}{1 + K_L C_e} \tag{3}$$

$$\text{Freundlich model}: Q_e = K_F C_e^{\frac{1}{n}} \tag{4}$$

$$\text{Temkin model}: Q_e = \frac{RT}{B} ln(AC_e) \tag{5}$$

$$\text{Redlich} - \text{Peterson model}: Q_e = \frac{K_R C_e}{1 + a_R C_e^g} \tag{6}$$

where Q_m (mg/g) is the theoretically calculated saturated adsorption capacity; K_L and K_F are constants in the Langmuir and Freundlich adsorption isotherm models, respectively; and n is the Freundlich coefficient denoting the adsorption strength. A and B are the constants. K_R and a_R are constants, and g is the exponent.

Adsorption kinetics experiments

Of ZnO/PUF-5, 3.5 g was immersed in 350 mL of phosphate-contaminated solution with an initial concentration of 200 mg/L and a pH of 6.3. The phosphate concentration was determined by adsorbing the supernatant for specific times (3 min, 5 min, 10 min, 20 min, 30 min, 60 min, 90 min, 120 min, 180 min, 240 min, 360 min, 540 min, 720 min, 960 min, 1200 min, 1440 min). After which the phosphate concentration of the tainted solution was ascertained by removing the supernatant. A series of adsorption kinetic studies were conducted to elucidate the adsorption mechanism of ZnO/PUF-5 on phosphate. The adsorption kinetics of phosphate on ZnO/PUF-5 were described using the pseudo-first-order kinetic model, the pseudo-second-order kinetic model, and intraparticle diffusion (Zhou et al.2018):

$$\text{Pseudo} - \text{first} - \text{order kinetic model}: \ln(Q_e - Q_t) = \ln Q_e - k_1 t \tag{7}$$

$$\text{Pseudo} - \text{second} - \text{order kinetic model}: \frac{t}{Q_t} = \frac{1}{k_2 Q_e^2} + \frac{t}{Q_e} \tag{8}$$

$$\text{Intrapaticle diffusion model } Q_t = k_1 t^{0.5} + C \tag{9}$$

The adsorption capacities at equilibrium and time t are Q_e (mg/g) and Q_t (mg/g). The rate constants for the quasi-first-order and quasi-second-order models are k_1 (min^{-1}) and k_2 (g/mg/min), respectively. k_i is the rate constant at stage i, and C is the correlation constant between the boundary layer and its thickness.

Effect of initial pH on adsorption performance

To investigate the impact of varying solution starting pH on phosphate adsorption performance on ZnO/PUF-5, potassium dihydrogen phosphate solution's pH was gone within the range of 3–11 using 0.10 mg/L NaOH and 0.10 mg/L HCl.

Column experiment

An adsorption column of 3 cm in inner diameter and 9 cm in height at room temperature was filled with a specific quantity of ZnO/PUF-5 to test the material's potential for practical applications. The adsorption column's pores were filled with 30 g of quartz sand. The diagram illustrating the configuration of the apparatus used in the column experiment is shown in Fig. S1. The study examined the adsorption capabilities of ZnO/PUF-5 in removing phosphate from contaminated liquid under several conditions, including varied flow rates, column heights, and starting concentrations. A peristaltic pump injects the tainted fluid into the column in a downward flow direction. Specimens were collected, centrifugated, and analyzed regularly to determine the phosphate concentration after treatment. When the contaminated solution's effluent concentration reaches 10% of the influent concentration ($C_t/C_o = 0.1$), the breakthrough time (t_b; min) is typically determined, and the column depletion (or saturation) time (t_s; min) may be computed when $C_t/C_o = 0.9$. The total adsorption capacity (qs; mg), unit adsorption at column depletion time (q_e; mg/g), total phosphate mass (m_s: mg) by adsorption column, empty bed contact time, and phosphoric acid removal rate of the adsorption column (η_s; %) (Mekonnen et al. 2021):

$$V_s = Qt_s \tag{10}$$

$$q_s = \frac{Q}{1000}\int_{t=0}^{t=t_s}(C_0 - C_t)dt \tag{11}$$

$$q_e = \frac{q_s}{m'} \tag{12}$$

$$m_s = \frac{C_0 Q t_s}{1000} \tag{13}$$

$$\eta_s = \frac{q_s}{m_s} \times 100\% \tag{14}$$

$$t_k = \frac{V_{bed}}{Q} \tag{15}$$

where Q is the velocity of flow of the contaminated liquid (mL/min), m' is the dry weight (g) of ZnO/PUF-5 in the adsorption column, and V_{bed} is the volume of the adsorption column (mL).

Data on dynamic adsorption were fitted using the Thomas, Yoon-Nelson, and Adams-Bohart models (Golie and Upadhyayula 2016):

$$\text{Thomas}: \ln\left(\frac{C_0}{C_t} - 1\right) = \frac{K_{Th} q_0 m}{Q} - K_{Th} C_0 t \tag{16}$$

$$\text{Yoon} - \text{Nelson}: \ln\left(\frac{C_t}{C_0 - C_t}\right) = K_{YN} t - \tau K_{YN} \tag{17}$$

$$\text{Adams} - \text{Bohart}: \ln\left(\frac{C_t}{C_0}\right) = K_{AB} C_0 t - K_{AB} N_0 \left(\frac{h}{U_0}\right) \tag{18}$$

where C_0 is the influent concentration (mg/L), C_t is the effluent concentration at time t (mg/L), K_{Th} is the Thomas model constant (mL/min·mg), q_0 is the Thomas dynamic adsorption capacity (mg/g), and m is the dry weight (g) of ZnO/PUF-5 material in the adsorption column. Q is the flow rate of the contaminated liquid (mL/min), t is the adsorption time (min), K_{YN} is the Yoon-Nelson model adsorption rate constant (min^{-1}), τ is the half-saturation, and adsorption time (min), K_{AB} is the Adams-Bohart model kinetic constant (L/mg·min), N_0 is the saturation concentration (mg/L), h is the column height of the adsorption column packing layer (cm), and so on. U_0 is the empty tower rate (cm/min), defined as the ratio of Q to A, where the cross-section area of A adsorption column (cm^2).

Results and discussion

Effect of ZnO dosage

Figure 3a illustrates the impact of ZnO dosage on the removal rate of phosphate, with an initial concentration of 100 mg/L. The removal rate of phosphate by pure PUF was shallow, amounting to just 4.26%. The ZnO dose increase increased the removal rate; nevertheless, the removal rate remained essentially constant at around 99% when the dosage exceeded or equaled 5.0 wt%. As shown in Fig. 3b, pure PUF had porosity and water adsorption of only 81.61% and 746.25%, respectively. With the increase in ZnO dosage to 5.0 wt%, the material porosity increased from 81.61 to 95.39%, and the water absorption from 746.25 to 2128.06%. Water absorption decreased from 2128.06 to 1124.76%, ZnO dosage rose 10.0%, and material porosity decreased from 95.39 to 93.33%. From this analysis, adding the correct quantity of ZnO will help the foam material's porosity and water absorption, which will enhance the material's adsorption capabilities.

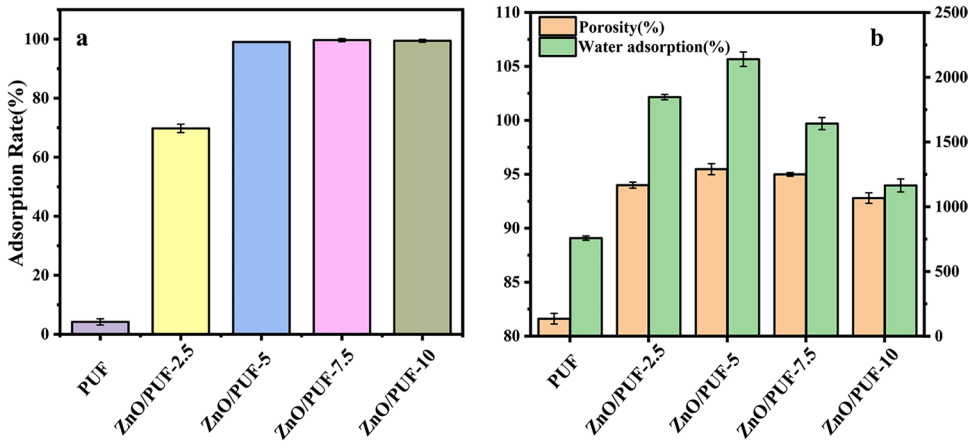

Fig. 3 **a** Adsorption rate of phosphate by ZnO/PUF-s fabricated with different ZnO dosages. **b** Porosity and water absorption of ZnO/PUF-s fabricated with different ZnO dosages

Characterization

ZnO powder with a particle size of around 0.26 μm was made using a straightforward co-precipitation technique (Fig. 4a). The pore size distribution of the pure polyurethane foam vesicles was found to be reasonably consistent, with an average pore size of around 0.72 mm, a smooth pore surface, and a limited quantity of micropores and macropores (Fig. 4b). The bubble pores of ZnO/PUF-5 displayed a wrinkled and rough surface structure when the proper amount of ZnO was added, with the average pore diameter rising to 1.12 mm (Fig. 4c). The SEM scan did not show ZnO directly, indicating that ZnO was deeply entrenched in the polyurethane foam matrix. Concurrently, the SEM pictures and the energy dispersive X-ray analysis findings (Fig. 4d) demonstrated that the elements of zinc (yellow area), carbon (red region), and oxygen (green part) were evenly distributed in ZnO/PUF-5.

As shown in Fig. 5, XRD analysis confirmed that ZnO filling into PUF was successful. The ZnO standard card (PDF#36–1451) matches the distinctive diffraction peaks at 2-Theta of 31°, 34°, and 36° in the XRD spectrum of ZnO/PUF-5, demonstrating the successful introduction of ZnO into the polyurethane foam. The N–H, C–H, and C = O stretching vibrations are responsible for the distinctive peaks in the PUF spectrum (Fig. 5b) at 3329 cm^{-1}, 2877 cm^{-1}, and 1711 cm^{-1}, respectively (Xie et al. 2019; Yuan et al. 2017). The vibrational peak seen at 1093 cm^{-1} corresponds to the C–O bending vibration. In addition, it can be shown that the C–N vibration generated by stretching is associated with the vibrational peak observed at 1462 cm^{-1}, indicating the successful formation of the carbamate bond in the polymer (Wei et al. 2022). The stretching and bending vibrations of

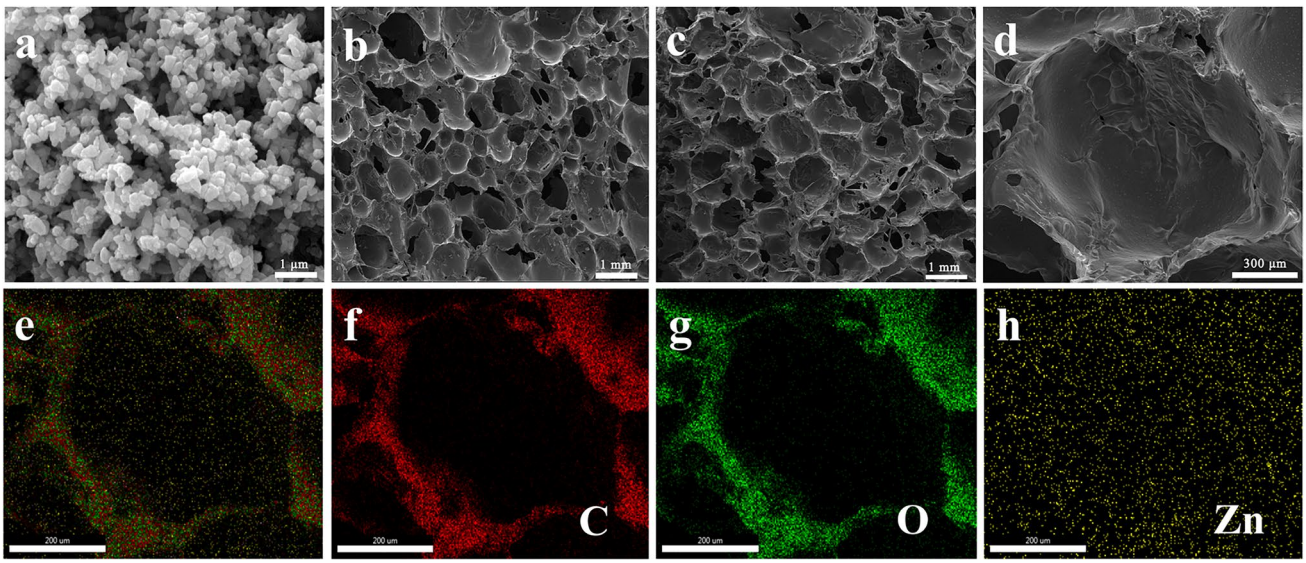

Fig. 4 **a** SEM images of ZnO, **b** SEM images of PUF, **c** and **d** SEM images of ZnO/PUF-5, **e**–**h** EDS mapping of ZnO/PUF-5

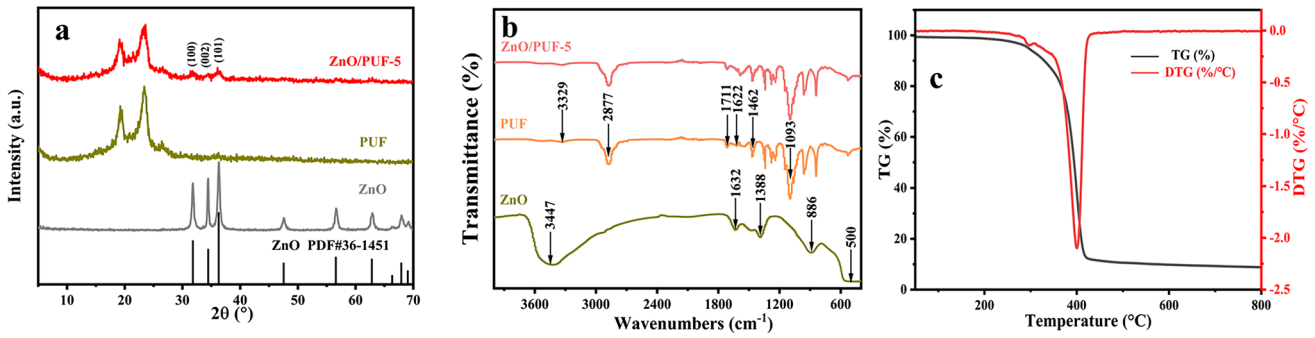

Fig. 5 **a** XRD pattern of ZnO/PUF-5 and **b** FTIR pattern of ZnO/PUF-5, **c** TG/DTG curve of ZnO/PUF-5

the –OH adsorbent on the surface of ZnO cause the spectral peaks in the ZnO spectra at 3447 cm^{-1} and 1632 cm^{-1} (Li et al. 2018). The vibration maxima at 886 cm^{-1} and 500 cm^{-1} indicate the bendable beats of the –OH and Zn–O in $Zn(OH)_2$. For ZnO/PUF-5, the characteristic peaks of PUF are preserved, and no prominent distinct peaks of ZnO are seen, which may be due to the small amount of ZnO added (5 wt%), and the characteristic peaks of polyurethane foam covering the distinct peaks of ZnO.

ZnO/PUF-5 undergoes three stages of thermal decomposition, as Fig. 5c illustrates. The first stage, which occurs at temperatures from 208 to 340 °C, has a specimen mass loss of approximately 13% and belongs to the stern section of thermal decomposition; the second stage, which occurs in a temperature vary of 340 to 420 °C, has a specimen mass loss of approximately 75% and belongs to the soft section of thermal decomposition; and the third stage, which occurs in the temperature. At 400 °C, the foam's weight loss rate reaches its highest, and at 797 °C, the polyurethane foam's residual mass is around 8%. Most of the leftover material is undecomposed ZnO since the thermal breakdown temperature of ZnO in ZnO/PUF-5 is more excellent than 2000 °C.

Adsorption properties in batch experiments

Adsorption isotherms

Adsorption isotherms were fitted using the Langmuir and Freundlich adsorption isotherm equations to examine the adsorption process, as seen in Fig. 6a, b. The Langmuir fitting correlation coefficient (R^2) shows a more excellent value than the Freundlich model (Table 2). This indicates that phosphate adheres to ZnO/PUF-5 by monolayer adsorption. The saturation adsorption capacity was calculated using the Langmuir isotherm model, and the result was 460.25 mg/g (calculated by ZnO). Temkin model fitting results indicate that the energy change of phosphates adsorbed on ZnO/PUF-5 is affected by temperature (Luo et al. 2024). In this work, the value of g is 0.954, close to 1 (Table 3). Therefore, the Redlich-Peterson isotherm constant agrees very well with the Langmuir isotherm, and the whole adsorption process is preferred to be described by the Langmuir model (Al-Ghouti et al. 2020).

In contrast, the most prevalent phosphate adsorbents summarized in Table 4 seldom achieve over 200 mg/g of uptake capacities even at optimal pH. It can be seen that the ZnO/PUF-5 obtained in this study has a significant effect on the purification of phosphate in water.

Adsorption kinetics

The completion of the adsorption process of phosphate at various temperatures was seen within a time frame of 1440 min, as shown in Fig. 6d. The adsorption process of phosphate by ZnO/PUF-5 may be categorized into three distinct stages, namely quick adsorption (0–360 min), slow adsorption (360–1200 min), and equilibrium adsorption (1200–1440 min), owing to the presence of a significant number of pore channels and a high pore size. Many active sites are extensively dispersed during the first phase, resulting in a rapid adsorption rate. As the adsorption process advances, an increasing number of active sites get occupied by phosphate, reducing available adsorption sites, and a subsequent plateau in the adsorption rate until equilibrium is reached. As the temperature rose within the range of 8–40 ℃, there was a corresponding progressive rise in the equilibrium adsorption capacity. In particular, the adsorption capacity increased from 360.10 to 394.63 mg/g (calculated by ZnO). This observation suggests that the rate of ionic diffusion is positively correlated with temperature, hence facilitating the adsorption process and enhancing the adsorption of phosphate by ZnO/PUF-5. The adsorption kinetics data were fitted to investigate the adsorption process further. Table 5 and Fig. 7b and c show the findings. The pseudo-second-order kinetic model at various temperatures has a higher correlation coefficient R^2 (0.992, 0.992, and 0.993) than the pseudo-first-order kinetic model, and the fitted adsorption capacity is more similar to the adsorption

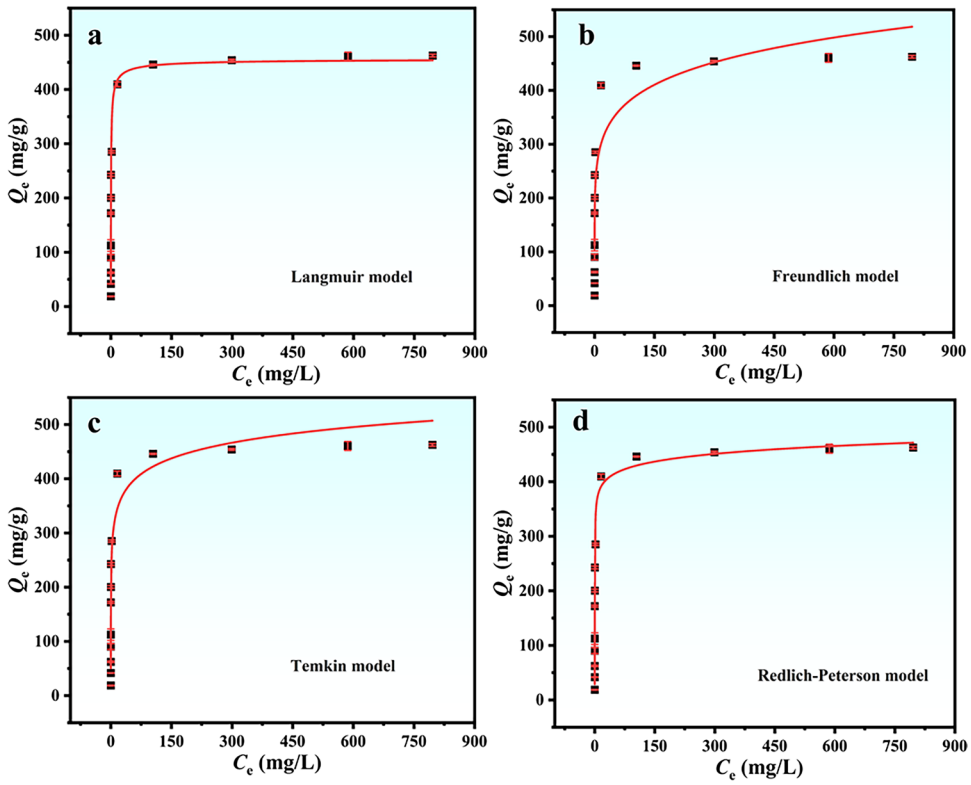

Fig. 6 **a** Langmuir isotherm model fitting. **b** Freundlich isotherm model fitting. **c** Temkin isotherm model fitting. **d** Redlich-Peterson isotherm model fitting

Table 2 Model parameters for the Langmuir and Freundlich adsorption isotherms

Sample	Langmuir			Freundlich		
	K_L (L/mg)	Q_e (mg/g)	R^2	K_F (mg/g)(L/mg)$^{1/n}$	$1/n$	R^2
ZnO/PUF	1.725	460.25	0.998	203.804	0.139	0.847

Table 3 Model parameters for the Temkin and Redlich-Peterson adsorption isotherms

Sample	Temkin			Redlich-Peterson			
	A (L/g)	B (kJ/mol)	R^2	K_R	a_R	g	R^2
ZnO/PUF	243.720	41.658	0.928	2322.770	6.653	0.955	0.969

Table 4 Comparison of phosphate uptake performance with different reported adsorbents

Adsorbent	Maximum adsorption capacity (mg/g)	Experimental conditions	Ref
ZnO/PUF-5	460.25	pH (5 ~ 6); 0.5 g/L; 25 ℃	This work
ZnO	163.40	pH 6.2 ± 0.1; 25 ℃	Shen et al. (2022)
CaZnAlZr-LDH	51.00	pH (7 ~ 8); 0.2 g/L; 25 ℃	Drenkova-Tuhtan et al. (2016)
ZnO-ZnAl	33.54	pH 7; 35 ℃	Liu et al. (2019)
La@ZIF-8	147.63	pH 6; 30 ℃	Li et al. (2020a)
ZIF-67	92.43	pH 6.82; 0.8 g/L; 25 ℃	Mazloomi et al. (2019)
Ce-MOF(500)	189.40	pH 6; 1 g/L; 25 °C	He et al. (2020)
NH_2-MIL-101(Fe)	124.38	pH 7;0.06 g/L; 20 ℃	Xie et al. (2017)
Al-MIL-101	90.00	pH 6; 0.2 g/L; 25 ℃	Li et al. (2020b)

capacity determined in the experiment. As a result, the phosphate adsorption by ZnO/PUF-5 is more in line with the chemisorption-dominated secondary kinetic process.

The intraparticle diffusion kinetic model was used to fit the adsorption kinetic data, assuming that the only rate-limiting step is intraparticle diffusion. In this work, the intraparticle diffusion kinetic model was used to fit the results as shown in Fig. 7d. All the plots do not pass through the origin but show a linear relationship, which suggests that intraparticle diffusion is not the only rate-controlling step in adsorption (Table 6).

Effect of initial pH value

The adsorption performance of the adsorbent on phosphate was observed to vary with the initial pH of the contaminated solution in the range of 3–11, as depicted in Fig. 8a. The adsorption capacity of the adsorbent for

Table 5 Parameters of pseudo-first-order and pseudo-second-order kinetic models

Temperatures (℃)	Pseudo-first-order			Pseudo-second-order		
	R^2	k_1 (1/min)	Q_e (mg/g)	R^2	k_2 (mg/g) (1/min)	Q_e (mg/g)
8 ℃	0.939	0.00382	290.89	0.992	0.00003	374.53
25 ℃	0.924	0.00283	261.34	0.992	0.00004	387.60
40 ℃	0.892	0.00308	246.87	0.993	0.00005	395.26

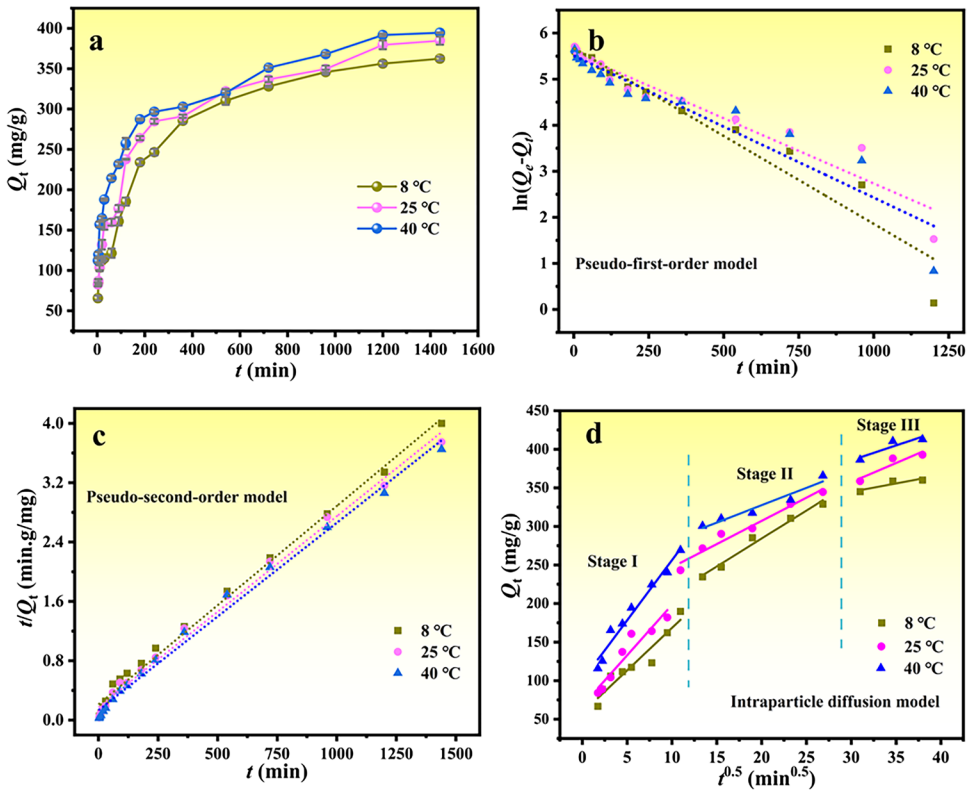

Fig. 7 **a** Adsorption kinetics of phosphate on ZnO/PUF-5. **b** Pseudo-first-order kinetic model fitting. **c** Pseudo-second-order kinetic model fitting. **d** Intraparticle diffusion model fitting

Table 6 Parameters for fitting the intraparticle diffusion model

Temperatures (℃)	Intraparticle diffusion model					
	k_1	R^2	k_2	R^2	k_3	R^2
8 ℃	10.998	0.920	7.245	0.981	2.176	0.829
25 ℃	12.745	0.911	5.876	0.964	4.845	0.871
40 ℃	14.847	0.969	4.294	0.938	3.682	0.839

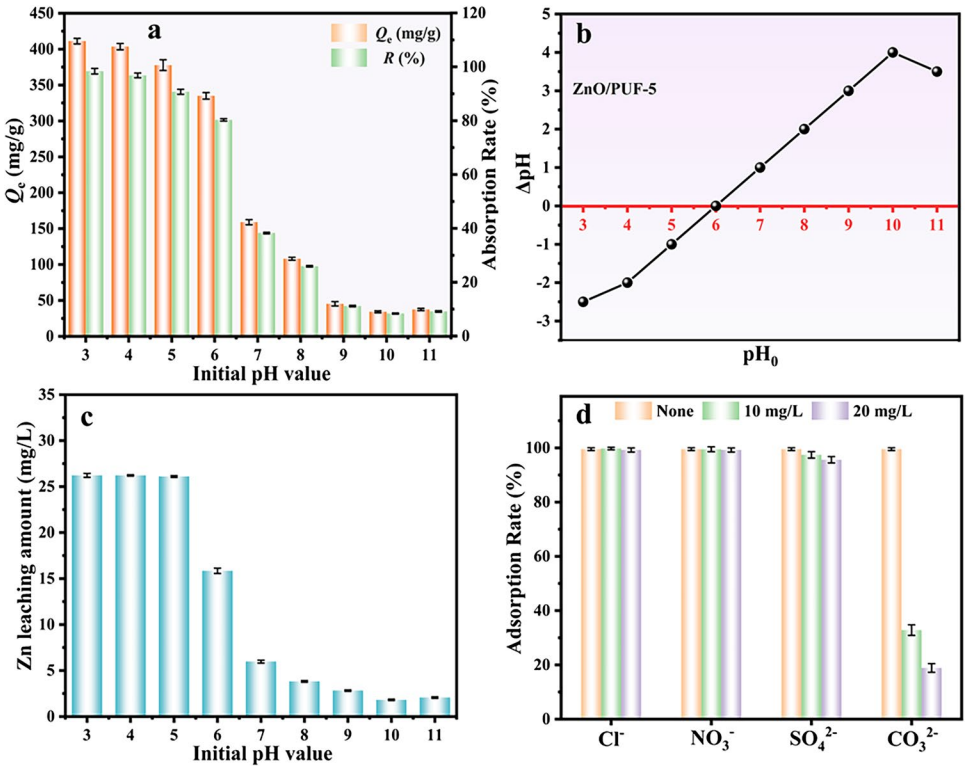

Fig. 8 **a** Effect of initial pH on phosphate adsorption capacity on ZnO/PUF-5. **b** Zero point charge of ZnO/PUF-5 surface**. c** Zinc leaching of adsorbents after phosphate adsorption at different pH values. **d** Effect of co-existing anions

phosphate diminishes as the initial pH value increases, with this effect being particularly pronounced when the pH value exceeds 6. The reason for the preferential binding of anions to the ZnO/PUF-5 material, when the solution pH is below the pHpzc (zero-point charge) value of 6 (Fig. 8b), is due to the positive surface charge acquired by ZnO/PUF-5 under such conditions. Hence, in instances when the pH level of the polluted solution falls below 6, the adsorption of phosphate by the ZnO/PUF-5 material is more advantageous. When the pH of the solution is higher than 6, ZnO/PUF-5's negatively charged surface makes it difficult to form bonds with phosphate anion, which causes a dramatic drop in the material's ability to adsorb phosphate. ZnO/PUF-5 has shown a greater affinity for phosphate across a more extensive pH range when compared to the analogous materials that have been reported. The initial pH value of the polluted solution within the scope of 3–6 may support over 335.82 mg/g of phosphate adsorption.

Figure 8c illustrates zinc leaching from the adsorbent following phosphate adsorption at various pH levels. Following adsorption, the concentration of zinc that leached from the solution was around 25.5 mg/L in the pH range of 3–5. As the pH increased, the amount of zinc that leached into the solution gradually reduced until it was below 5 mg/L.

Effect of co-existing anions

At a phosphate concentration of 30 mg/L, the effects of several common anions (Cl^-, NO_3^-, SO_4^{2-}, and CO_3^{2-}) on the adsorption performance of ZnO/PUF-5 at varied concentrations were examined. The findings were displayed in Fig. 8d, which demonstrated that there was little to no change in the rates at which Cl^- and NO_3^- adsorption occurred on phosphate. The adsorption rate of Cl^- and NO_3^- on phosphate was essentially unaffected; the adsorption rate of phosphate showed a modest drop but remained above 95% with an increase in SO_4^{2-} concentration; and the removal of phosphate was more affected by the presence of CO_3^{2-}. The adverse effects were $Cl^- < NO_3^- < SO_4^{2-} < CO_3^{2-}$, in decreasing order.

Adsorption mechanism

The scanned pictures of ZnO/PUF-5 before and after phosphate adsorption are shown in Fig. 9a–f. Before adsorption, the vesicles of the material exhibited a surface structure that was folded and rough. However, after adsorption, the pores of ZnO/PUF-5 expanded, resulting in numerous fiber-like network structures. Additionally, many spherical substances resembling tremella were observed on the surface of the vesicles (Fig. S2a). In the analysis of the EDS patterns of

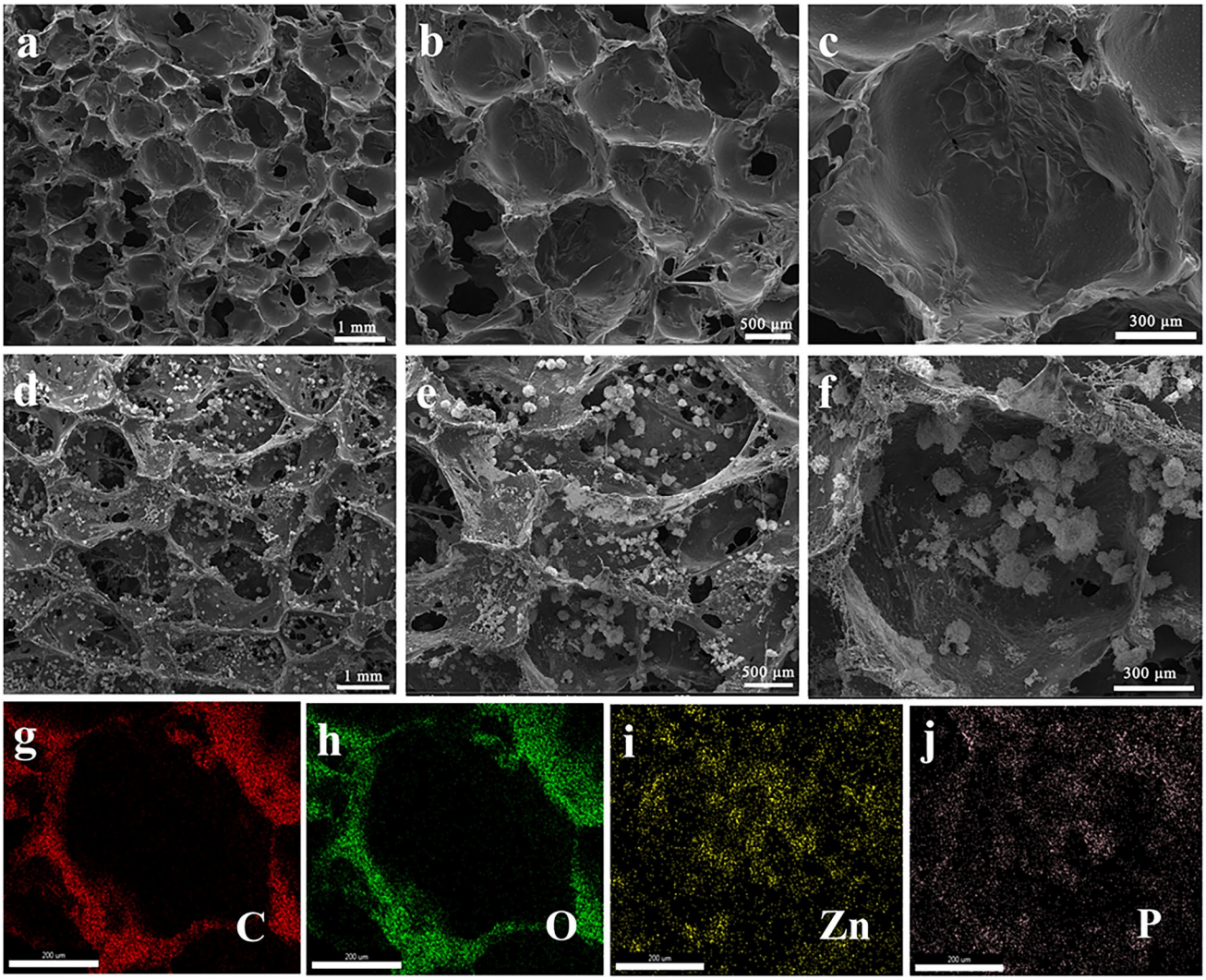

Fig. 9 **a–c** SEM images of ZnO/PUF-5 before p adsorption, **d–f** SEM images of ZnO/PUF-5 after p adsorption, and **g–j** EDS mapping of ZnO/PUF-5 after p adsorption

ZnO/PUF-5 before adsorption (Fig. 4e), it was observed that a significant presence of P elements was detected in the adsorbed samples. This finding suggests that ZnO/PUF-5 effectively adsorbed phosphate.

Furthermore, Fig. 9j reveals a substantial overlap between Zn and P elements in the adsorbed samples, indicating that phosphate likely primarily adhered to the ZnO powder. The FTIR analysis conducted before and after the adsorption of phosphate by the ZnO/PUF-5 did not exhibit significant changes, as depicted in Fig. 10a. Additionally, the FTIR spectra of pure ZnO powder, both before and after phosphate adsorption, displayed the absence of vibrational peaks corresponding to –OH in $Zn(OH)_2$, as shown in Fig. S3, specifically at 886 cm^{-1}. Conversely, three new vibrational peaks emerged at 943 cm^{-1}, 1008 cm^{-1}, and 1120 cm^{-1}, which correspond to the vibrational peaks of the P–O bond in the phosphate (Yang et al. 2015). This observation suggests that adsorption depletes the –OH groups and generates P–O bonds. Therefore, it is further explained that ZnO plays a significant role in phosphate adsorption in composite materials.

XPS analysis was performed to further confirm the adsorption mechanism of ZnO/PUF-5 on phosphate. The outcomes are shown in Fig. 10b–f. The appearance of P2p peaks in the XPS spectra (Fig. 10b) demonstrated that the phosphate had adsorbed on ZnO/PUF-5. Figure 8c displays the XPS-Zn 2p spectra of the material before and after adsorption. Before adsorption, the Zn 2p spectra showed two different peaks: Zn $2p_{1/2}$ and Zn $2p_{3/2}$, respectively, with energies of 1021.6 eV and 1044.6 eV. Following adsorption, the Zn 2p spectra showed no change in the typical peaks associated with Zn. The materials' C 1 s spectra, as seen in Fig. 8d, show a noticeable difference before and after adsorption.

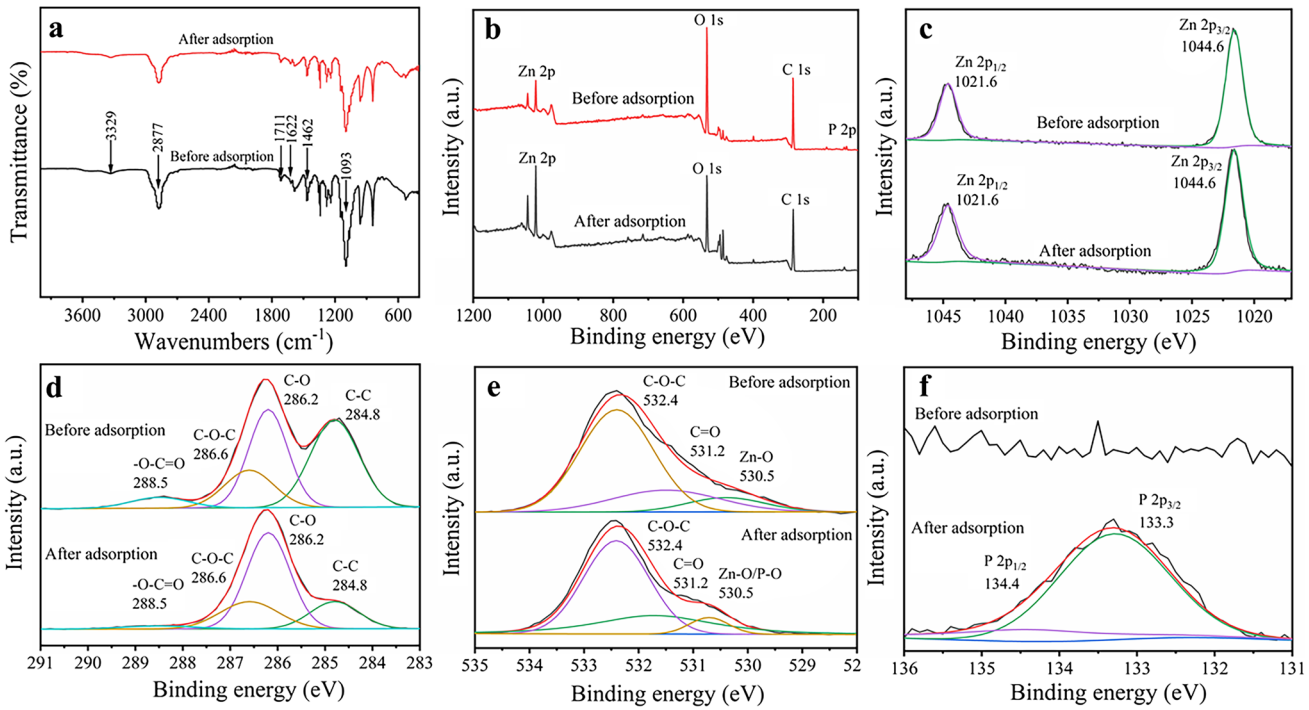

Fig. 10 **a** FTIR spectra of ZnO/PUF-5 before and after p adsorption, **b–f** XPS spectra of ZnO/PUF-5 before and after p adsorption (**b** total spectrum; **c** Zn 2p; **d** C 1 s; **e** O 1 s; **f** P 2p)

Notably, the intensity of the characteristic peaks associated with the C–C bonds of the materials experienced a reduction after adsorption. This observation suggests that the structure of the materials underwent a certain degree of impairment during the adsorption process. Figure 10e displays the O 1 s spectra of the materials before and following adsorption. The energy level of 530.5 eV corresponds to the Zn–O bond in ZnO and the P–O bond in phosphate (Wang and Xiang 2014). The C = O and C–O–C bonds in urethane are shown by the unique peaks at 531.5 eV and 532.4 eV, respectively. Notably, the intensity of the characteristic peaks at 530.5 eV increased after adsorption, suggesting the presence of adsorbed phosphate on the materials. Figure 9f presents the XPS-P 2p spectra of the materials before and following adsorption. Notably, distinctive peaks following adsorption at 133.3 eV and 134.4 eV, respectively, correspond to P $2p_{3/2}$ and P $2p_{1/2}$. These peaks signify the presence of $H_2PO_4^-$ and HPO_4^- species (Xie et al. 2014), indicating substantial phosphate adsorption onto the surface of ZnO/PUF-5.

Based on the research above, in conjunction with the findings about adsorption thermodynamics, adsorption kinetics, and the zero-point charge pH of ZnO/PUF-5, it can be deduced that the primary mechanism by which ZnO/PUF-5 adsorbs phosphates is via ligand exchange and electrostatic interactions, the specific descriptions are as follows.

Ligand exchange:

$$\mathrm{ZnO/PUF-OH + H_2PO_4^- \rightarrow ZnO/PUF-H_2PO_4 + OH^-} \quad (19)$$

$$\mathrm{2ZnO/PUF-OH + HPO_4^{2-} \rightarrow (ZnO/PUF)_2-HPO_4 + 2OH^-} \quad (20)$$

Electrostatic interactions:

$$\mathrm{ZnO/PUF-OH_2^+ + H_2PO_4^- \rightarrow ZnO/PUF-OH_2 \cdots H_2PO_4} \quad (21)$$

$$\mathrm{2ZnO/PUF-OH_2^+ + HPO_4^{2-} \rightarrow (ZnO/PUF-OH_2)_2 \cdots HPO_4} \quad (22)$$

The schematic representation of this adsorption mechanism is illustrated in Fig. 11.

Adsorption properties in column experiments

Setting the initial pollutant concentration and column height allowed for the investigation of the impact of flow rate on the adsorption process. The data shown in Fig. 12a indicates a correlation between the steepening of the breakthrough curves and the leftward shift of the breakthrough and column depletion points. This correlation suggests that as the flow rate rises, there is a decrease in the time needed to reach the breakthrough and column depletion points. The observed decrease in breakthrough time and column depletion time as the flow rate of the contaminated liquid increased aligns

with the removal rate constants (K_{TH}, K_{YN}, and K_{AB}) estimated for the three chosen models (Table S2, Fig. S4). This suggests that higher flow rates are associated with accelerated saturation rates.

The breakthrough curve exhibited a deceleration as the height of the adsorption column packing increased from 4.5 to 9.0 cm (Fig. 12b), resulting in a rightward shift of the breakthrough point and column depletion point. This shift indicates that the time required to reach the breakthrough point and column depletion point tended to increase with the increase in column height (Unuabonah et al. 2010). This observation suggests that the prolongation of breakthrough and column depletion times at higher bed heights can be attributed to the expansion of the mass transfer region (Table 5). Furthermore, it can be inferred that using higher quality ZnO/PUF-5 (i.e., higher column height) leads to a larger surface area of the adsorbent and an increased number of active sites (Table 7).

The column's height and flow rate were determined to be 9 cm and 1.0 mL/min, respectively. The influence of

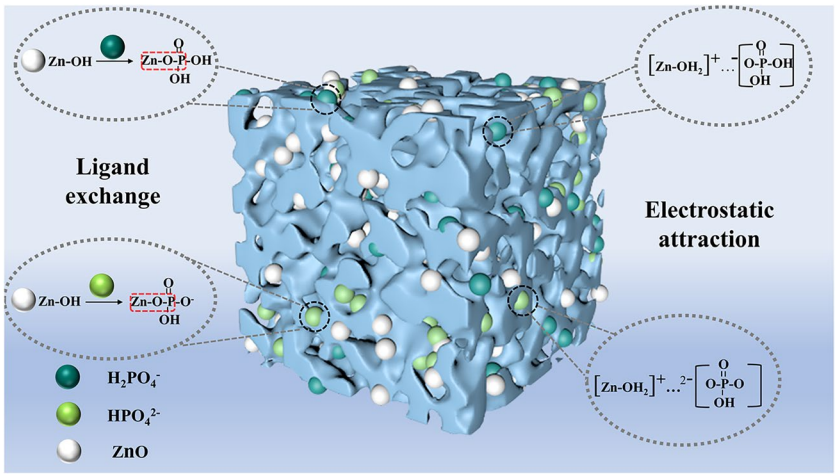

Fig. 11 Adsorption mechanism diagram

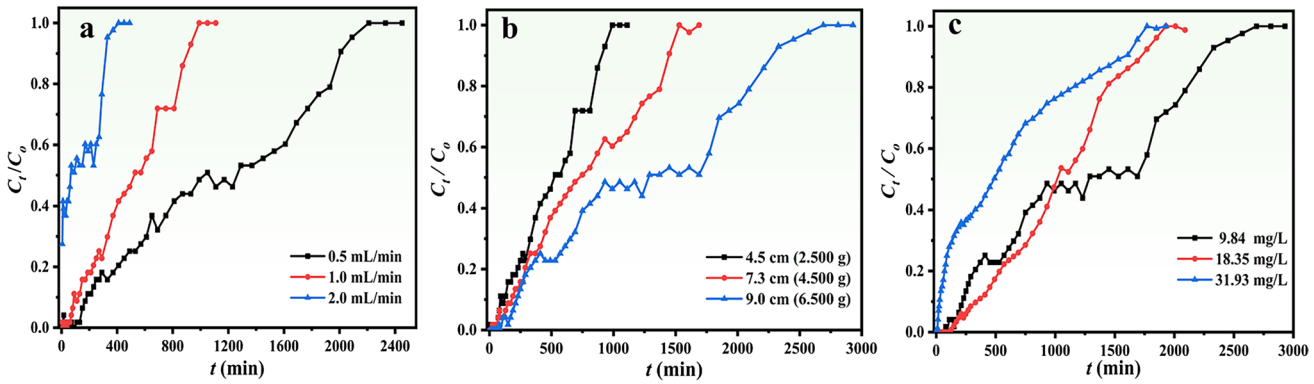

Fig. 12 **a** Penetration curves at different flow rates. **b** Penetration curves at different column heights. **c** Penetration curves at different concentrations

Table 7 Adsorption parameters of ZnO/PUF-5 on phosphate in fixed bed with different parameters

Number	Q (mL/min)	h (cm)	C_0 (mg/L)	t_s (min)	q_s (mg)	q_e (mg/g)	m_s (mg)	η_s (%)	t_k (min)
1	0.5	4.5	9.84	2010	5.62	44.94	9.89	56.81	63.62
2	1.0	4.5	9.84	930	5.08	40.65	9.15	55.54	31.81
3	2.0	4.5	9.84	330	2.71	21.64	6.49	41.67	15.9
4	1.0	7.3	9.84	1450	7.67	34.06	14.27	53.73	51.6
5	1.0	9.0	9.84	2330	12.38	38.08	22.93	53.98	63.62
6	1.0	9.0	18.35	1770	18.72	57.59	32.49	57.62	63.62
7	1.0	9.0	31.93	1610	18.93	58.25	51.41	36.82	63.62

the starting concentration on the process of adsorption was investigated. Figure 10 displays the breakthrough curve. Changes in the starting concentration significantly impact the breakthrough and column depletion time. The reduction in breakthrough and column depletion time was seen when the initial concentration of the intake-contaminated solution rose, and this may be attributed to the quick saturation of adsorption sites on the surface of ZnO/PUF-5. When the initial concentrations are elevated, the observed phenomena may be attributed to the substantial concentration gradient between the liquid and solid phases. This phenomenon often leads to an increased diffusivity or mass transfer driving force during phosphate adsorption (Salman et al. 2011).

Conclusion

In summary, ZnO/PUF composites were successfully made using a one-step foaming technique to remove phosphate from water effectively. The findings indicated that the ZnO powder exhibited a homogeneous dispersion inside the PUF material, effectively addressing the agglomeration and separation challenges encountered with the ZnO powder in aqueous solutions. The PUF porous matrix has high permeability and exhibits outstanding hydrophilicity. The equally distributed ZnO inside the matrix offers more active sites. Consequently, these combined factors contribute to a substantial enhancement in the purification efficiency of phosphate in aqueous solutions. The saturated phosphate adsorption could reach 460.25 mg/g after adsorption at an initial pH of 6.3 of the contaminated liquid and at 25 °C for 24 h. Compared with many reported adsorbents, ZnO/PUF has a higher adsorption capacity. Secondly, ZnO/PUF is promising as an adsorbent material that is easy to synthesize, low-cost, and easy to separate from water after adsorption. The composites exhibited high phosphorus removal performance in the pH range of 3–6. The results of the column experiments, which examined the breakthrough curves at different flow rates, column heights, and initial phosphate concentrations, demonstrated that the composite material could continue to perform well during the dynamic adsorption process and could be used in real-world applications to treat wastewater that contains phosphorus. These benefits indicate that the composite material has many potential uses and will provide a new avenue for efficiently removing phosphate from water.

Supplementary Information The online version contains supplementary material available at https://doi.org/10.1007/s11356-024-34235-4.

Author contribution Yang Cao: conceptualization and writing—original draft.

Peicong Zhang and Yi Huang: writing—review and editing.

Suying Chen, Junfeng Li, Haiying Du, Wentao Zhang, Xianfei Chen, and Daming Yu: methodology and investigation.

Funding This study was supported by the Science and Technology Department of Sichuan Province (2021JDTD0013), the Major Science and Technology Project of Tibetan Autonomous Region (XZ202201ZD0004G06), and the Everest Scientific Research Program (80000-2023ZF11405).

Declarations

Ethical approval No animal studies are presented in this manuscript. No human studies are presented in this manuscript. No potentially identifiable human images or data are presented in this study.

Consent to participate All authors consent to participate on this research project.

Consent for publication All authors consent to publishing this manuscript.

Conflict of interest The authors declare no competing interests.

References

Al-Ghouti, Mohammad A, Da'ana DA (2020) Guidelines for the use and interpretation of adsorption isotherm models: a review. J Hazard Mater 393:122383. https://doi.org/10.1016/j.jhazmat.2020.122383

Cheng S, Chen Q, Xia H et al (2018) Microwave one-pot production of ZnO/Fe_3O_4/activated carbon composite for organic dye removal and the pyrolysis exhaust recycle. J Clean Prod 188:900–910. https://doi.org/10.1016/j.jclepro.2018.03.308

Cordell D, Drangert J, White S (2009) The story of phosphorus: global food security and food for thought. Glob Environ Chang 19(2):292–305. https://doi.org/10.1016/j.gloenvcha.2008.10.009

Cramer M (2010) Phosphate as a limiting resource: introduction. Plant Soil 334(1–2):1–10. https://doi.org/10.1007/s11104-010-0497-9

Das NC, Rahman MM, Kabir SF (2023) Preparation of novel clay/chitosan/ZnO bio-composite as an efficient adsorbent for tannery wastewater treatment. Int J Biol Macromol 249. https://doi.org/10.1016/j.ijbiomac.2023.126136

Drenkova-Tuhtan A, Schneider M, Mandel K et al (2016) Influence of cation building blocks of metal hydroxide precipitates on their adsorption and desorption capacity for phosphate in wastewater—a screening study. Colloids Surf A 488:145–153. https://doi.org/10.1016/j.colsurfa.2015.10.017

Feng L, Zhang Q, Ji F et al (2022) Phosphate removal performances of layered double hydroxides (LDH) embedded polyvinyl alcohol/lanthanum alginate hydrogels. Chem Eng J 430. https://doi.org/10.1016/j.cej.2021.132754

Golie WM, Upadhyayula S (2016) Continuous fixed-bed column study for the removal of nitrate from water using chitosan/alumina composite. J Water Process Eng 12:58–65. https://doi.org/10.1016/j.jwpe.2016.06.007

He J, Xu Y, Wang W et al (2020) Ce(III) nanocomposites by partial thermal decomposition of Ce-MOF for effective phosphate adsorption in a wide pH range. Chem Eng J 379. https://doi.org/10.1016/j.cej.2019.122431

He Z, Honeycutt C (2005) A modified molybdenum blue method for orthophosphate determination suitable for investigating enzymatic

hydrolysis of organic phosphates. Commun Soil Sci Plant Anal 36(9–10):1373–1383. https://doi.org/10.1081/css-200056954
Hong X, Zhu S, Xia M et al (2022) Investigation of the efficient adsorption performance and adsorption mechanism of 3D composite structure La nanosphere-coated Mn/Fe layered double hydrotalcite on phosphate. J Colloid Interface Sci 614:478–488. https://doi.org/10.1016/j.jcis.2022.01.149
Huang W, Yu X, Tang J et al (2015) Enhanced adsorption of phosphate by flower-like mesoporous silica spheres loaded with lanthanum. Microporous Mesoporous Mater 217:225–232. https://doi.org/10.1016/j.micromeso.2015.06.031
Hwang S (2020) Eutrophication and the ecological health risk. Int J Environ Res Public Health 17(17). https://doi.org/10.3390/ijerph17176332
Jung K, Kim K, Jeong T et al (2016) Influence of pyrolysis temperature on characteristics and phosphate adsorption capability of biochar derived from waste-marine macroalgae (Undaria pinnatifida roots). Bioresour Technol 200:1024–1028. https://doi.org/10.1016/j.biortech.2015.10.016
Kumar PS, Korving L, van Loosdrecht M et al (2019) Adsorption as a technology to achieve ultra-low concentrations of phosphate: research gaps and economic analysis. Water Res X 4. https://doi.org/10.1016/j.wroa.2019.100029
Lalley J, Han C, Li X et al (2016) Phosphate adsorption using modified iron oxide-based sorbents in lake water: kinetics, equilibrium, and column tests. Chem Eng J 284:1386–1396. https://doi.org/10.1016/j.cej.2015.08.114
Li N, Tian Y, Zhao J et al (2018) Ultrafast selective capture of phosphorus from sewage by 3D Fe_3O_4@ZnO via weak magnetic field enhanced adsorption. Chem Eng J 341:289–297. https://doi.org/10.1016/j.cej.2018.02.029
Li J, Chang H, Li Y et al (2020a) Synthesis and adsorption performance of La@ZIF-8 composite metal–organic frameworks. RSC Adv 10(6):3380–3390. https://doi.org/10.1039/c9ra10548d
Li S, Lei T, Jiang F et al (2020b) Tuning the morphology and adsorption capacity of Al-MIL-101 analogues with Fe^{3+} for phosphorus removal from water. J Colloid Interface Sci 560:321–329. https://doi.org/10.1016/j.jcis.2019.10.077
Liu Z, Lu Y, Li X et al (2019) Adsorption of phosphate from wastewater by a ZnO-ZnAl hydrotalcite. Int J Environ Anal Chem 99(14):1415–1433. https://doi.org/10.1080/03067319.2019.1622696
Luo Z, Zhu S, Liu Z et al (2015) Study of phosphate removal from aqueous solution by zinc oxide. J Water Health 704–713. https://doi.org/10.2166/wh.2015.210
Luo Q, Liu P, Bi L et al (2024) Selective and efficient removal of ciprofloxacin from water by bimetallic MOF beads: mechanism quantitative analysis and dynamic adsorption. [J] Sep Purif Technol 332. https://doi.org/10.1016/j.seppur.2023.125832
Madhusudan P, Lee C, Kim J-O (2024) Hierarchical ZnO/$ZnFe_2O_4$ yolk-shell adsorbent as a promising material for phosphate recovery and adsorption of organic pollutants from the simulated wastewater. Sep Purif Technol 348. https://doi.org/10.1016/j.seppur.2024.127598
Mazloomi S, Yousefi M, Nourmoradi H et al (2019) Evaluation of phosphate removal from aqueous solution using metal organic framework; isotherm, kinetic and thermodynamic study. J Environ Health Sci Eng 17(1):209–218. https://doi.org/10.1007/s40201-019-00341-6
Mekonnen D, Alemayehu E, Lennartz B (2021) Fixed-bed column technique for the removal of phosphate from water using leftover coal. Materials 14(19). https://doi.org/10.3390/ma14195466
Ramasahayam S, Guzman L, Gunawan G et al (2014) A comprehensive review of phosphorus removal technologies and processes. J Macromol Sci Part A 51(6):538–545. https://doi.org/10.1080/10601325.2014.906271
Ren L, Gao X, Zhang X et al (2022) Stable and recyclable polyporous polyurethane foam highly loaded with UIO-66-NH_2 nanoparticles for removal of Cr(VI)in wastewater. Polymer 255. https://doi.org/10.1016/j.polymer.2022.125117
Salman J, Njoku V, Hameed B (2011) Batch and fixed-bed adsorption of 2,4-dichlorophenoxyacetic acid onto oil palm frond activated carbon. Chem Eng J 174(1):33–40. https://doi.org/10.1016/j.cej.2011.08.024
Shen Y, Yuan Z, Cheng F et al (2022) Preparation and characterization of ZnO/graphene/graphene oxide/multi-walled carbon nanotube composite aerogels. Front Chem 10. https://doi.org/10.3389/fchem.2022.992482
Smith V, Schindler D (2009) Eutrophication science: where do we go from here? Trends Ecol Evol 24(4):201–207. https://doi.org/10.1016/j.tree.2008.11.009
Unuabonah E, Olu-Owolabi B, Fasuyi E et al (2010) Modeling of fixed-bed column studies for the adsorption of cadmium onto novel polymer–clay composite adsorbent. J Hazard Mater 179(1–3):415–423. https://doi.org/10.1016/j.jhazmat.2010.03.020
Wang J, Xiang L (2014) Formation of ZnO rods with varying diameters from ε-$Zn(OH)_2$. J Cryst Growth 401:279–284. https://doi.org/10.1016/j.jcrysgro.2014.01.070
Wei Y, Liang X, Wu H et al (2021) Efficient phosphate removal by dendrite-like halloysite-zinc oxide nanocomposites prepared via noncovalent hybridization. Appl Clay Sci 213. https://doi.org/10.1016/j.clay.2021.106232
Wei X, Chen D, Wang L et al (2022) Carboxylate-functionalized hollow polymer particles modified polyurethane foam for facile and selective removal of cationic dye. Appl Surf Sci 579. https://doi.org/10.1016/j.apsusc.2021.152153
Xie J, Wang Z, Lu S et al (2014) Removal and recovery of phosphate from water by lanthanum hydroxide materials. Chem Eng J 254:163–170. https://doi.org/10.1016/j.cej.2014.05.113
Xie F, Zhang T, Bryant P et al (2019) Degradation and stabilization of polyurethane elastomers. Prog Polym Sci 90:211–268. https://doi.org/10.1016/j.progpolymsci.2018.12.003
Xie Q, Li Y, Lv Z et al (2017) Effective adsorption and removal of phosphate from aqueous solutions and eutrophic water by Fe-based MOFs of MIL-101. Sci Rep 7(1). https://doi.org/10.1038/s41598-017-03526-x
Yan L, Xu Y, Yu H et al (2010) Adsorption of phosphate from aqueous solution by hydroxy-aluminum, hydroxy-iron and hydroxy-iron–aluminum pillared bentonites. J Hazard Mater 179(1–3):244–250. https://doi.org/10.1016/j.jhazmat.2010.02.086
Yang W, Huo M, Liu J et al (2015) Study of phosphate removal from aqueous solution by zinc oxide. J Water Health 13(3):704–713. https://doi.org/10.2166/wh.2015.210
Yuan D, Zhang T, Guo Q et al (2017) A novel hierarchical hollow SiO_2 @MnO_2 cubes reinforced elastic polyurethane foam for the highly efficient removal of oil from water. Chem Eng J 327:539–547. https://doi.org/10.1016/j.cej.2017.06.144
Yuchi A, Ogiso A, Muranaka S et al (2003) Preconcentration of phosphate and arsenate at sub-ng ml−1 level with a chelating polymer-gel loaded with zirconium(IV). [J] Anal Chim Acta 494(1–2):81–86. https://doi.org/10.1016/s0003-2670(03)00901-2
Zhang X, Shen J, Ma Y et al (2020c) Highly efficient adsorption and recycle of phosphate from wastewater using flower-like layered double oxides and their potential as synergistic flame retardants. J Colloid Interface Sci 562:578–588. https://doi.org/10.1016/j.jcis.2019.11.076
Zhang M, Song T, Zhu C et al (2020a) Roles of nitrate recycling ratio in the A2/O-MBBR denitrifying phosphorus removal system for high-efficient wastewater treatment: performance comparison, nutrient mechanism and potential evaluation. J Environ Manag 270. https://doi.org/10.1016/j.jenvman.2020.110887

Zhang Q, Li J, Lin Q et al (2020b) A stiff ZnO/carbon foam composite with second-level macroporous structure filled ZnO particles for heavy metal ions removal. Environ Res 188. https://doi.org/10.1016/j.envres.2020.109698

Zhou K, Wu B, Su L et al (2018) Enhanced phosphate removal using nanostructured hydrated ferric-zirconium binary oxide confined in a polymeric anion exchanger. Chem Eng J 345:640–647. https://doi.org/10.1016/j.cej.2018.01.091